

above examine relatively simple binary systems, where only a single type of DNA sticky end duplex is created. However, because of the polyvalent nature of the DNA-NPs and the base sequence programmability of DNA, one is not necessarily restricted to a single type of favorable particle interaction in a given lattice. By cofunctionalizing a nanoparticle with different linkers that contain different base sequences, multiple sequence-specific DNA duplex interactions are possible (Fig. 4A). This is an inherent distinction and potential advantage of using a sequence-programmable linker such as DNA, as opposed to entropy- or charge-dominated assembly processes.

This rule was tested by cofunctionalizing a nanoparticle with two different linkers: one that bore a self-complementary sticky end, and one that bore a sticky end sequence complementary to the sticky ends of a second particle. In this system, the cofunctionalized particle (blue particle, Fig. 4A) exhibited an attractive force with respect to all particles encountered in the system, whereas the second particle (red particle, Fig. 4A) was only attracted to the first particle type. When the hydrodynamic radius size ratio of the two NPs was  $\sim 0.3$  to  $0.4$ , the sticky ends were presented at the correct distances from the particle surface to form a NaCl lattice (Fig. 4B); that is, the self-complementary and non-self-complementary linkers were both at a position to form duplexes in this crystallographic arrangement. Furthermore, when the inorganic core sizes were the same on both DNA-NPs, the particles formed a simple cubic lattice, as defined by the positions of the inorganic cores (Fig. 4C). Although NaCl and simple cubic structures are presented as the first examples of this multivalent strategy, one can envision even more sophisticated and complex systems (such as lattices with three or more nanoparticle components) using multiple DNA-programmed NP interactions.

We have presented a set of basic design rules for synthesizing a diverse array of nanoparticle superlattices using DNA as a synthetically programmable linker. These rules provide access to an easily tailorable, multifaceted design space in which one can independently dictate the crystallographic symmetry, lattice parameters, and particle sizes within a lattice. This in turn enables the synthesis of many different nanoparticle superlattices that cannot be achieved through other methodologies. Indeed, superlattices that do not follow the well-known hard-sphere packing parameter rules defined by Schiffrin and co-workers (6) and Murray and co-workers (8, 24) can easily be assembled as thermodynamically stable structures over a range of nanoparticle sizes and lattice parameters. The understanding gained from the use of these rules will both inform and enable future assembly efforts, allowing for the construction of new crystallographic arrangements that have emergent properties for use in the fields of plasmonics (14, 25, 26), photonics (27), catalysis (28, 29), and potentially many others.

## References and Notes

1. L. Pauling, *The Nature of the Chemical Bond* (Cornell Univ. Press, Ithaca, NY, ed. 3, 1960).
2. C. A. Mirkin, R. L. Letsinger, R. C. Mucic, J. J. Storhoff, *Nature* **382**, 607 (1996).
3. S.-J. Park, A. A. Lazarides, J. J. Storhoff, L. Pesce, C. A. Mirkin, *J. Phys. Chem. B* **108**, 12375 (2004).
4. S. Y. Park *et al.*, *Nature* **451**, 553 (2008).
5. D. Nykypanchuk, M. M. Maye, D. van der Lelie, O. Gang, *Nature* **451**, 549 (2008).
6. C. J. Kiely, J. Fink, M. Brust, D. Bethell, D. J. Schiffrin, *Nature* **396**, 444 (1998).
7. A. M. Kalsin *et al.*, *Science* **312**, 420 (2006); 10.1126/science.1125124.
8. E. V. Shevchenko, D. V. Talapin, N. A. Kotov, S. O'Brien, C. B. Murray, *Nature* **439**, 55 (2006).
9. S. Srivastava *et al.*, *Science* **327**, 1355 (2010); 10.1126/science.1177218.
10. S. Wong, V. Kitaev, G. A. Ozin, *J. Am. Chem. Soc.* **125**, 15589 (2003).
11. Y. Zhao *et al.*, *Nat. Mater.* **8**, 979 (2009).
12. C.-L. Chen, N. L. Rosi, *Angew. Chem. Int. Ed.* **49**, 1924 (2010).
13. Z. Nie, A. Petukhova, E. Kumacheva, *Nat. Nanotechnol.* **5**, 15 (2010).
14. M. R. Jones, K. D. Osberg, R. J. Macfarlane, M. R. Langille, C. A. Mirkin, *Chem. Rev.* **111**, 3736 (2011).
15. R. J. Macfarlane *et al.*, *Proc. Natl. Acad. Sci. U.S.A.* **106**, 10493 (2009).
16. R. J. Macfarlane *et al.*, *Angew. Chem. Int. Ed.* **49**, 4589 (2010).
17. M. R. Jones *et al.*, *Nat. Mat.* **9**, 913 (2010).
18. H. Xiong, D. van der Lelie, O. Gang, *Phys. Rev. Lett.* **102**, 015504 (2009).
19. See supporting material on Science online.
20. L. V. Woodcock *et al.*, *Nature* **385**, 141 (1997).
21. O. Zhou *et al.*, *Nature* **351**, 462 (1991).
22. V. A. Bloomfield, D. M. Crothers, I. Tinoco, *Nucleic Acids: Structures, Properties, and Functions* (University Science Books, Sausalito, CA, 2000).
23. A. V. Tkachenko, *Phys. Rev. Lett.* **89**, 148303 (2002).
24. M. I. Bodnarchuk, M. V. Kovalenko, W. Heiss, D. V. Talapin, *J. Am. Chem. Soc.* **132**, 11967 (2011).
25. K. L. Kelly, E. Coronado, L. L. Zhao, G. C. Schatz, *J. Phys. Chem. B* **107**, 668 (2002).
26. J. A. Fan *et al.*, *Science* **328**, 1135 (2010).
27. K. J. Stebe, E. Lewandowski, M. Ghosh, *Science* **325**, 159 (2009).
28. A. T. Bell, *Science* **299**, 1688 (2003).
29. J. Grunes, J. Zhu, E. A. Anderson, G. A. Somorjai, *J. Phys. Chem. B* **106**, 11463 (2002).

**Acknowledgments:** Supported by the Defense Research & Engineering Multidisciplinary University Research Initiative of the Air Force Office of Scientific Research and by the U.S. Department of Energy Office of Basic Energy Sciences [award DE-SC0000989; Northwestern University (NU) Non-equilibrium Energy Research Center] (C.A.M. and G.C.S.); a National Security Science and Engineering Faculty Fellowship from the U.S. Department of Defense (C.A.M.); a NU Ryan Fellowship (R.J.M.); and a NU Ryan Fellowship and a NSF Graduate Research Fellowship (M.R.J.). Portions of this work were carried out at the DuPont-Northwestern-Dow Collaborative Access Team (DND-CAT) beamline located at Sector 5 of the Advanced Photon Source (APS). DND-CAT is supported by E. I. DuPont de Nemours & Co., Dow Chemical Company, and the state of Illinois. Use of the APS was supported by the U.S. Department of Energy, Office of Science, Office of Basic Energy Sciences, under contract DE-AC02-06CH11357. The transmission electron microscope work was carried out in the EPIC facility of the NU Atomic and Nanoscale Characterization Experimental Center, which is supported by NSF-NSEC, NSF-MRSEC, Keck Foundation, the state of Illinois, and NU. Ultrathin sectioning was carried out at the NU Biological Imaging Facility, supported by the NU Office for Research.

## Supporting Online Material

www.sciencemag.org/cgi/content/full/334/6053/204/DC1  
Materials and Methods  
SOM Text  
Figs. S1 to S31  
Tables S1 and S2  
References (30–44)  
29 June 2011; accepted 25 August 2011  
10.1126/science.1210493

# Conical Intersection Dynamics in NO<sub>2</sub> Probed by Homodyne High-Harmonic Spectroscopy

H. J. Wörner,<sup>1,2\*</sup> J. B. Bertrand,<sup>1</sup> B. Fabre,<sup>3</sup> J. Higuette,<sup>3</sup> H. Ruf,<sup>3</sup> A. Dubrouil,<sup>3</sup> S. Patchkovskii,<sup>1</sup> M. Spanner,<sup>1</sup> Y. Mairesse,<sup>3</sup> V. Blanchet,<sup>4</sup> E. Mével,<sup>3</sup> E. Constant,<sup>3</sup> P. B. Corkum,<sup>1</sup> D. M. Villeneuve<sup>1</sup>

Conical intersections play a crucial role in the chemistry of most polyatomic molecules, ranging from the simplest bimolecular reactions to the photostability of DNA. The real-time study of the associated electronic dynamics poses a major challenge to the latest techniques of ultrafast measurement. We show that high-harmonic spectroscopy reveals oscillations in the electronic character that occur in nitrogen dioxide when a photoexcited wave packet crosses a conical intersection. At longer delays, we observe the onset of statistical dissociation dynamics. The present results demonstrate that high-harmonic spectroscopy could become a powerful tool to highlight electronic dynamics occurring along nonadiabatic chemical reaction pathways.

The outcome of chemical reactions is determined by the valence electronic structure of molecules. Therefore, the elucidation of elementary reaction mechanisms requires an understanding of the valence electron dynamics. Recently developed techniques that are efficient

in probing valence electron dynamics include attosecond transient absorption (1), extreme ultraviolet photoelectron spectroscopy (XUV-PES) (2), high-order harmonic spectroscopy (HHS) (3–5) and strong-field ionization (6). Both time-resolved PES (7) and time-resolved HHS are

sensitive to valence electron dynamics through the molecular photoionization matrix elements.

Electronic dynamics in molecules are particularly challenging to observe when they are strongly coupled to nuclear dynamics. Such situations often arise in polyatomic molecules where conical intersections between the potential energy surfaces induce very rapid radiationless transitions at particular nuclear configurations (see inset of Fig. 1) (8, 9). These features channel electronic excitation into atomic motion in such diverse contexts as the primary steps of vision (10) and the dynamics underlying electron transfer and the photostability of DNA bases (11).

Here, we show that high-harmonic spectroscopy reveals the variations in electronic character during the conical intersection dynamics and the subsequent dissociation of nitrogen dioxide ( $\text{NO}_2$ ). We chose  $\text{NO}_2$ , a radical, because of its model status for theories of unimolecular dissociation (12–14) and conical intersection dynamics (15–19). Our results translate the previously recognized sensitivity of HHS to electronic structure into a tool for elucidating chemical reaction dynamics.

High-harmonic spectroscopy can be factored into three steps: removal of an electron by an intense femtosecond laser field, acceleration of the electron in the laser field, and photorecombination (20, 21). Each step contributes an amplitude and a phase to the emitted XUV radiation (22–24, 20, 25). The measurement relies on a coherent detection scheme in a transient grating geometry, using unexcited molecules as a local oscillator (4, 5). It is thus sensitive to both amplitude and phase of the photorecombination matrix elements, a quantity that has recently attracted a lot of interest (26, 27). Time-resolved PES is thus related to time-resolved PES but differs in its sensitivity to the continua associated with different ionic states. PES projects the molecular wave packet onto a set of ionic states, influenced by resonances, Franck-Condon factors, and dissociative ionization. HHS involves recombination from an energetic continuum electron with one or a few of the lowest ionic states that were selected by tunneling ionization.

A schematic representation of the potential energy surfaces of  $\text{NO}_2$  is shown in Fig. 1. In the  $\tilde{X}^2A_1$  electronic ground state,  $\text{NO}_2$  possesses a bent equilibrium geometry and the dominant electronic configuration in the two highest occupied orbitals is  $(b_2)^2(a_1)^1$ . Single-photon absorption at 400 nm excites the molecule to the  $\tilde{A}^2B_2$

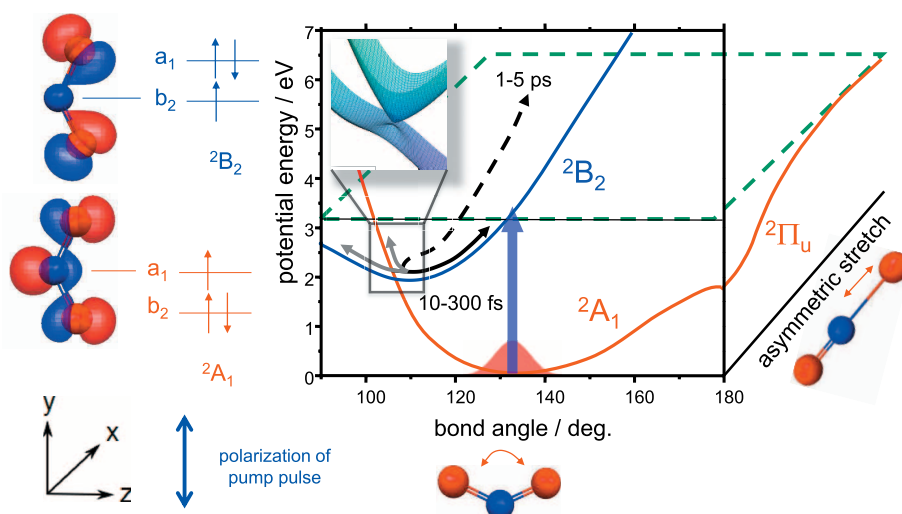


**Fig. 1.** Schematic representation of the potential energy surfaces of the ground  $\tilde{X}^2A_1$  and excited  $\tilde{A}^2B_2$  electronic states of  $\text{NO}_2$ . The dominant electronic configuration in the two highest-lying molecular orbitals is shown for each state on the left. The orbitals are represented by isoamplitude surfaces of the wave function with color-coding of the sign. After excitation by a 400-nm pump pulse (blue arrow), the wave packet initially moves along the bending coordinate, crosses the conical intersection (shown in the top left inset) several times during the first 100 fs, and spreads along the asymmetric-stretch coordinate. Wave-packet population that has returned to the ground electronic state and possesses an energy above 3.1155 eV (green dashed line) dissociates on the picosecond time scale (dashed arrow).

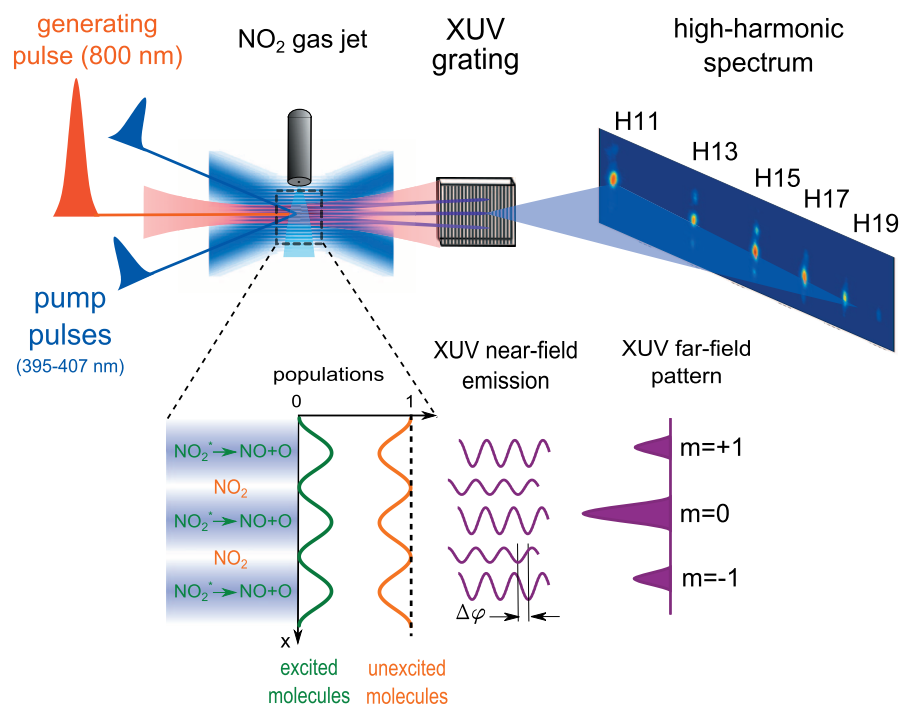


**Fig. 2.** Experimental setup for high-harmonic transient grating spectroscopy as first described in (4). The transient grating creates a spatially modulated population of excited molecules accompanied by a depletion of the unexcited molecules. The periodic structure results in a modulation of amplitude and phase of the XUV emission in the near field that leads to first-order diffraction in the far field. An XUV grating disperses the radiation in one dimension while the beam freely diverges in the other dimension. With  $r(\cos(kx) + 1)$  being the spatially modulated excitation fraction, the signal in  $m = 0$  is given by  $I_{m=0} = |(1-r)d_g e^{i\phi_g} + r d_e e^{i\phi_e}|^2$  and that in  $m = \pm 1$  by  $I_{m=\pm 1} = \frac{r^2}{4} |d_e e^{i\phi_e} - d_g e^{i\phi_g}|^2$ , where the symbols are defined in the text relating to Eq. 1.

<sup>1</sup>Joint Laboratory for Attosecond Science, National Research Council of Canada and University of Ottawa, 100 Sussex Drive, Ottawa, Ontario, Canada K1A 0R6. <sup>2</sup>Laboratorium für Physikalische Chemie, Eidgenössische Technische Hochschule Zürich, Wolfgang-Pauli-Strasse 10, 8093 Zürich, Switzerland. <sup>3</sup>Centre Lasers Intenses et Applications, Université de Bordeaux, CEA, CNRS, UMR5107, 351 Cours de la Libération, 33405 Talence, France. <sup>4</sup>Laboratoire Collisions Agrégats Réactivité (IRSAMC), UPS, Université de Toulouse, F-31062 Toulouse, France and CNRS, UMR 5589, F-31062 Toulouse, France

\*To whom correspondence should be addressed. E-mail: woerner@phys.chem.ethz.ch

state of dominant configuration  $(b_2)^1(a_1)^2$ . The  $\tilde{A}^2B_2$  excited state forms a conical intersection with the ground state (see inset of Fig. 1). Wave-packet calculations have shown that within the first femtoseconds after excitation, the nuclear wave packet moves along the bending coordinate toward the conical intersection, where it can either cross the intersection and remain on the same diabatic surface or else stay in the upper cone of the intersection and thus change the diabatic surface (gray arrows in Fig. 1) (15–18). After a few hundred femtoseconds, the nuclear wave packet returns to the electronic ground state through internal conversion. If the energy of the absorbed photon lies above the first dissociation limit at 3.1155 eV (397.95 nm) (all quoted wavelengths are vacuum values), the molecule dissociates into NO ( $X^2\Pi_G$ ) and O ( $^3P_J$ ) on the picosecond time scale (dotted arrow in Fig. 1). Previous studies using laser-induced fluorescence have characterized the picosecond dissociation in detail (14, 28). However, the femtosecond conical intersection dynamics has been largely obscured by competing multiphoton processes (19), requiring elaborate coincidence detection methods (29).

The experimental setup is illustrated in Fig. 2. We excite NO<sub>2</sub> in a transient grating formed from two synchronized 400-nm laser pulses and probe its dynamics by high-harmonic generation from an 800-nm, 32-fs laser pulse (4, 30). The excitation pulses are generated either in a 2-mm-thick  $\beta$ -barium borate (BBO) crystal, providing 160-fs pulses of 1-nm spectral width tunable from 395 to 407 nm or in a 100- $\mu$ m-thick BBO crystal, giving 40-fs pulses of 5-nm spectral width. The combination of the transient grating with an XUV monochromator allows us to spectrally resolve the high harmonics (H11 to H21 in this experiment) and to measure both the undiffracted ( $m = 0$ ) and diffracted ( $m = \pm 1$ ) components of each harmonic order. The signal observed in  $m = 0$  is equivalent to a measurement done in a collinear pump-probe geometry, whereas the diffracted signal results from an interference between equal populations of excited and unexcited molecules (4).

We first discuss the picosecond photo-dissociation dynamics, which show that our measurement is dominated by single-photon absorption. The measurements were done with the 160-fs pulses, but we have obtained fully consistent results with the 40-fs pulses. The dynamics observed after excitation by pump pulses centered at 407 or 397.2 nm are shown in Fig. 3, A and C, respectively. Figure 3A shows a step-like decrease of the undiffracted XUV radiation and a corresponding increase of the diffracted intensity. The total ion yield, measured simultaneously and shown in Fig. 3B, increases, whereas the high-order harmonic signal decreases; this indicates a destructive interference between harmonics emitted by the ground state and those emitted by the excited state (4, 5). In this scan, performed with a 200-fs delay step, there is no

signature of any regular dynamics. Figure 3, C and D, however, show exponential growth or decay on the picosecond time scale, following the step-like variations.

The combined information from Fig. 3 shows that the step-like response to excitation below threshold characterizes electronic excitation without dissociation (Fig. 3, A and B), whereas the exponential variation of the signal in Fig. 3, C and D shows the unimolecular decomposition of NO<sub>2</sub>. To quantify these observations, we introduce a simple model. When excitation takes

place below threshold, the radiated XUV field can be described as in Eq. 1

$$E_{\text{XUV}}(\Omega) = (1 - r)d_g e^{i\phi_g} + r d_e e^{i\phi_e} \quad (1)$$

where  $r$  is the spatially modulated fraction of excited molecules, and  $d_g$ ,  $d_e$  and  $\phi_g$ ,  $\phi_e$  are the high-harmonic amplitudes and phases of the ground or excited molecular states, respectively. When the excitation frequency exceeds threshold, the excited molecules can undergo dissociation into NO(<sup>2</sup> $\Pi$ )+O(<sup>3</sup>P) that, together, emit harmonics

**Table 1.** Molecular parameters for strong-field ionization and high-harmonic generation, determined by fitting Eqs. 1 and 2 to the experimental data shown in Fig. 3, A to D. The excitation fraction  $r$  has been determined from the experimental parameters as described in the text.

Species	$r$	$iI_i$	H13		H15		H17	
			$d/d_g$	$ \phi - \phi_g (\text{rad})$	$d/d_g$	$ \phi - \phi_g (\text{rad})$	$d/d_g$	$ \phi - \phi_g (\text{rad})$
NO <sub>2</sub> <sup>+</sup> (407 nm)	0.15	4.5	3.0	2.03	2.3	2.02	1.2	2.24
NO <sub>2</sub> <sup>+</sup> (397 nm)	0.15	4.5	3.2	1.94	2.1	1.92	1.1	4.22
NO + O (397 nm)	0.15	2.3	6.1	2.09	4.1	2.00	1.4	1.87

$\tau = 2.71 \pm 0.15$  ps

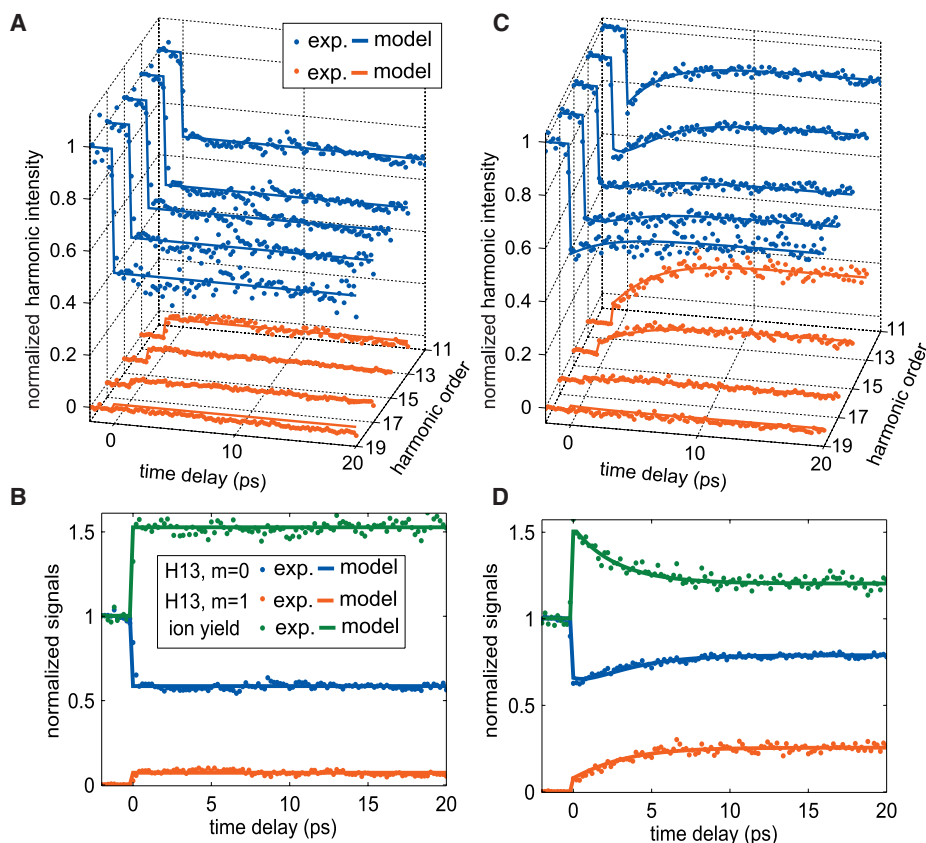


**Fig. 3.** High-harmonic and ion yields as a function of delay between two synchronized near-UV pump pulses setting up a transient grating and an 800-nm probe pulse generating high harmonics in the excited sample. (A) The yield of diffracted (red dots) and undiffracted (blue dots) high-harmonic signals, normalized to the undiffracted signal at negative pump-probe delays, for excitation by 407-nm pump pulses. The full lines represent the results of the theoretical model described in the text. (B) H13,  $m = 0$ , and  $m = 1$  from (A) together with the total ion yield measured in parallel to the experiment (green dots) and the theoretical model (green line). (C and D) The same observables as (A and B), but for a pump pulse centered at 397.2 nm. Polarization of pump and probe are parallel. The typical pump energy is 10  $\mu$ J to minimize multiphoton processes.

with a resultant amplitude  $d_t$  and phase  $\phi_t$ . The radiated XUV field is then given by Eq. 2

$$E_{\text{XUV}}(\Omega, t) = (1 - r)d_g e^{i\phi_g} + r e^{-t/\tau} d_e e^{i\phi_e} + r(1 - e^{-t/\tau}) d_t e^{i\phi_t} \quad (2)$$

where  $t$  is the time elapsed since excitation and  $\tau$  is the time constant of the unimolecular dissociation.

To extract the relevant parameters from the measurement, both the diffracted and undiffracted high-harmonic signals are normalized by the signal measured in the absence of excitation (namely,  $|d_g|^2$ ). We calculate the excited state fraction from the measured pulse energy, focal spot size, and the known absorption cross section of  $\text{NO}_2$  and determine the unknown parameters in a global nonlinear least-squares fit. The determined parameters are given in Table 1, and the corresponding fit is shown as full lines in Fig. 3, A to D. The total ion yield is represented by equations similar to Eqs. 1 and 2 but with phases set to zero.

The global fit to all high-harmonic orders and ion signals in Fig. 3, B and D, provides a

time constant  $\tau = 2.71 \pm 0.15$  ps, in agreement with the 2.78 ps measured previously at room temperature (14). The deep modulation of the signals demonstrates that the probed dynamics are dominated by one-photon absorption, which is in general difficult to achieve in femtosecond time-resolved measurements on molecules because of multiphoton processes (19). The strong-field ionization probability of vibrationally excited  $\text{NO}_2$  molecules in the electronic ground state is larger than that of unexcited molecules [vertical ionization potential ( $I_p$ ) =

11.2 eV] by a factor of  $\left(\frac{I_p}{I_{p0}}\right) \approx 4.5$ . The ionization

rate of  $\text{NO} + \text{O}$  (dominated by  $\text{NO}$  because the vertical  $I_p$  values are 9.2 and 13.8 eV, respectively) exceeds that of the unexcited molecules by a factor of  $\approx 2.3$ . The relative high-harmonic amplitudes are larger for the excited molecules, especially for low harmonic orders, and the phase shift is substantial, as expected from the observed destructive interference. The relative amplitudes for the  $\text{NO} + \text{O}$  pair decrease particularly fast

with increasing harmonic order, as expected from the lower cutoff of the harmonic emission from  $\text{NO}$ . We thus conclude that the observed high-harmonic signal is dominated by single-photon excitation, in contrast to previous femtosecond time-resolved measurements that reported oscillatory components of periods in the range of 500 to 850 fs (31–33). The latter were indeed attributed to multiphoton excitations to higher-lying electronic states that would not emit high harmonics owing to their low binding energies.

In the following, we exploit this property to investigate the hitherto unobserved femtosecond dynamics of  $\text{NO}_2$  in the  $\tilde{A}^2B_2$  state. These measurements were done with 40-fs excitation pulses centered at 401 nm. The experimental results measured with cross-polarized laser pulses are shown in Fig. 4, A and B. Fig. 4A shows the undiffracted and diffracted signals measured in harmonics 11 through 17 (blue and red dots, respectively), and Fig. 4B shows the same quantities for H15 and H16 (green line). The latter allows an accurate determination of the zero time delay and the cross-correlation function (34). Whereas the  $m = 0$  order decreases smoothly over the duration of the cross correlation, the diffracted order ( $m = 1$ ) increases and reaches a maximum at a pump-probe delay of 35 fs. The diffracted signal subsequently decreases and reaches a minimum around 70 fs, followed by another maximum at 130 fs. Further modulations with decreasing contrast are observed at longer pump-probe delays. As we show and discuss in fig. S2 and the accompanying text, no modulations are observed in parallel polarization.

These oscillations, observed in the diffracted XUV radiation, are a fingerprint of the electronic dynamics of the molecule taking place around the conical intersection, as illustrated schematically in Fig. 4D. In the bright zones of the transient grating, the electronic character of the excited molecules oscillates between  $\tilde{X}^2A_1$  and  $\tilde{A}^2B_2$ . When the molecule is in the  $\tilde{X}^2A_1$  state, the near-field variation of the high-harmonic emission is much smaller for most molecular geometries than when it is in the  $\tilde{A}^2B_2$  state, which we detect as a variation of the intensity of diffracted radiation [see section VI of the supporting online material (SOM)].

To rationalize these observations, we introduce a simple model based on diabatic electronic states and coordinate-independent transition moments (more detailed calculations are given in the SOM). The total radiated XUV field is the coherent sum of contributions from the unexcited molecules (subscript g) and excited molecules in the two diabatic  $\tilde{A}^2B_2$  and  $\tilde{X}^2A_1$  states (Eq. 3)

$$E_{\text{XUV}}(\Omega, t) = [1 - r(t)]d_g e^{i\phi_g} + r_{\tilde{X}}(t)d_{\tilde{X}} e^{i\phi_{\tilde{X}}} + r_{\tilde{A}}(t)d_{\tilde{A}} e^{i\phi_{\tilde{A}}} \quad (3)$$

where  $r(t) = r_{\tilde{X}}(t) + r_{\tilde{A}}(t)$  is the total fraction of excited molecules before dissociation takes

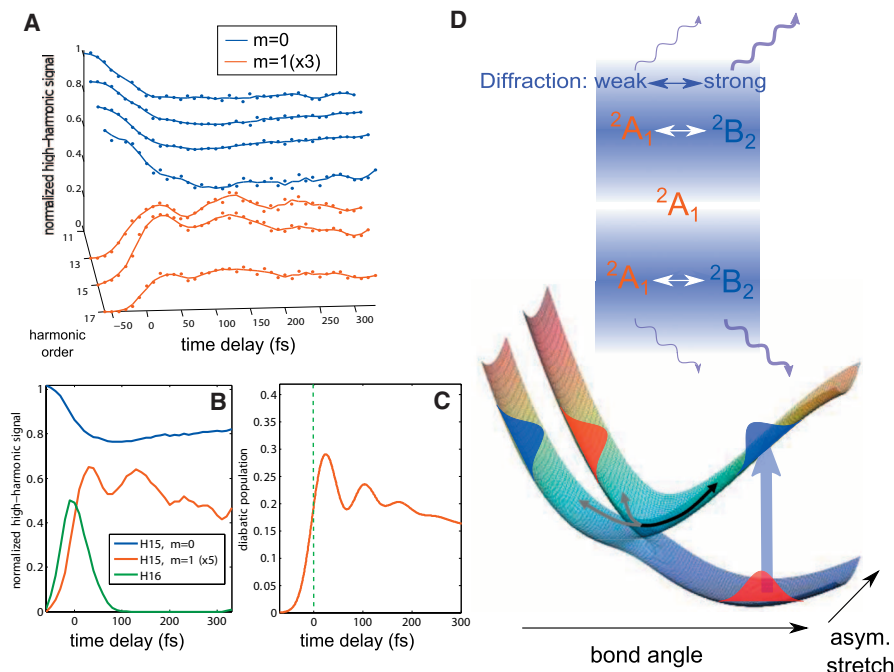


**Fig. 4.** (A) The high-harmonic yields after excitation by a pair of 10- $\mu\text{J}$ , 401-nm laser pulses in the undiffracted (blue) and diffracted orders (red) of the odd harmonics (H11 to H17). Experimental data points appear as dots and a three-point-smoothed version as lines. (B) The undiffracted (blue) and diffracted orders of H15 (red) and H16 (green line). (C) The diabatic excited state population from (17) convoluted with a 50-fs Gaussian cross-correlation function. (D) Illustration of how high-harmonic transient-grating spectroscopy probes the electronic character of the molecule during the conical intersection dynamics. The top illustrates the spatial intensity structure of the transient grating. The bottom shows schematically the lowest two potential energy surfaces of  $\text{NO}_2$ . When the molecule is in the excited diabatic state (represented as a blue wave packet), the high-harmonic emission differs significantly from the unexcited ( $^2A_1$ ) molecules, leading to a large variation of high-harmonic amplitude and phase across the transient grating and thus to strong diffraction. When population is transferred into the ground diabatic state (red wave packet), the modulation depth of high-harmonic amplitude and phase across the transient grating, and therefore the diffracted intensity, decreases.

place. The intensity of the diffracted light is thus given by Eq. 4 (4)

$$I_{m=1}(\Omega, t) = \frac{1}{4} |r_{\tilde{A}}(t)(d_{\tilde{A}}e^{i\tilde{\omega}_A} - d_g e^{i\tilde{\omega}_g}) + r_{\tilde{X}}(t)(d_{\tilde{X}}e^{i\tilde{\omega}_X} - d_g e^{i\tilde{\omega}_g})|^2 \quad (4)$$

The high-harmonic amplitude is determined by the probabilities of ionization and recombination. The phase is determined by the phase accumulated by the bound state ( $I_p \tau$ ), and the recombination phase (24), where  $\tau$  stands for the transit time of the electron in the continuum ( $\sim 1$  to 1.7 fs). To the first order, ionization from either  $\tilde{A}^2B_2$  or  $\tilde{X}^2A_1$  involves the removal and recombination of an  $a_1$  electron in the cross-polarized case (Fig. 1). The main difference is due to the  $I_p \tau$  phase. The ground-state channel  $^1A_1 \leftarrow ^2A_1$  has an  $I_p$  of 11.2 eV, whereas the main excited-state ionization channel  $^3B_2 \leftarrow ^2B_2$  has an  $I_p$  that varies between 9.8 eV and 13.2 eV as a function of the bending coordinate. The relative phase difference  $\Delta I_p \tau$  stays close to zero for the  $\tilde{X}^2A_1$  state, whereas it is significantly larger (between 1 and 3 radians) for most geometries of the  $\tilde{A}^2B_2$  state. Hence, in Eq. 4,  $|d_{\tilde{A}}e^{i\tilde{\omega}_A} - d_g e^{i\tilde{\omega}_g}| \gg |d_{\tilde{X}}e^{i\tilde{\omega}_X} - d_g e^{i\tilde{\omega}_g}|$  and the time dependence of the diffracted signal will be dominated by HHG emission from the  $\tilde{A}^2B_2$  state. It is thus sensitive to the temporal variation of the population in the  $\tilde{A}^2B_2$  state, as illustrated in Fig. 4D. This conclusion is also supported by the detailed calculations described in the SOM.

The observed polarization dependence of the oscillations is a consequence of the electronic symmetries. Photoexcited molecules have their  $y$  axis (O-O axis) parallel to the polarization of the exciting field (Fig. 1). In the cross-polarized experiment, the emission from excited molecules is thus dominated by those probed along their  $z$  axis ( $C_2$  axis). The same orientation also dominates the emission from the unexcited molecules, resulting in a sensitivity to the diabatic electronic state of the excited molecule ( $^2B_2$  versus  $^2A_1$ ). In the case of parallel polarizations, the photoexcited molecules are being probed along their  $y$  axis, whereas the unexcited molecules are probed along their  $z$  axis. Therefore, the emission from excited molecules in both diabatic states differs significantly from that of the unexcited molecules, and the amount of diffracted light is sensitive only to the total population of excited molecules.

Because the electronic dynamics between  $\tilde{X}^2A_1$  and  $\tilde{A}^2B_2$  have not been observed experimentally before, we compare the measurements to recent quantum dynamical calculations on  $\text{NO}_2$  (17, 18). These three-dimensional wave packet calculations have predicted characteristic oscillations in the diabatic populations over the first few hundred femtoseconds. The diabatic  $\tilde{A}^2B_2$  population  $r_{\tilde{A}}(t)$ , convoluted with a 50-fs Gaussian cross-correlation function, is shown in Fig. 4C. Both the overall behavior and the distinct features observed in the diffracted high-harmonic signal are present in the calculated

diabatic state population. The first maximum occurs at a delay of 26 fs, the first minimum at 68 fs, and the second maximum at 106 fs. The modulations in the diffracted signal thus reflect the diabatic state population dynamics. Considering the complexity of the problem and the simplicity of our model, the agreement is remarkable. To exclude the possibility that the observed modulations result from a change of the strong-field-ionization rate of the molecule as a function of the nuclear coordinates, we have also measured the total ion yield in parallel to the high-harmonic yield and have not observed any modulation on top of the smooth increase (see fig. S3 and accompanying text).

Comparing the experimental and theoretical results, we can draw a qualitative picture of the evolution of the electronic structure of the molecule as it crosses the conical intersection. Photoexcitation prepares the wave packet on the upper diabatic state as shown in Fig. 4D. When it first approaches the conical intersection, it has little expansion along the asymmetric stretch coordinate (the  $b_2$  mode responsible for vibronic coupling), and thus most of the amplitude traverses the intersection and remains on the same diabatic state [80% according to the wave packet calculation (17)]. This fraction, the diabatic wave packet, returns to the conical intersection with a significant spread along the bond-stretching coordinate, resulting in a strong transfer to the ground diabatic state. This leads to the first minimum in the diabatic state population around 60 fs. After two or three periods of motion along the bending coordinate, wave packet components from diabatic and adiabatic traversals interfere with each other and extend so significantly along the symmetric and asymmetric stretch coordinates that no appreciable motion of the wave packet average position can be defined for times longer than 200 fs (15, 17).

High-harmonic spectroscopy is a powerful probe of electronic dynamics in nonadiabatic processes. The homodyne interference of species in different electronic states has enabled us to distinguish multiple photochemical pathways—electronic excitation to bound states versus excitation followed by dissociation. The coherence of the high-harmonic emission also enabled us to extract amplitudes and phases of the various species occurring in the photochemical transformation and to learn how to interpret them. Temporal variations in the dominant electronic configuration of the photoexcited wave packet are manifested in a polarization dependence of the pump-probe signal, which is expected to be a powerful property in future studies of electronic dynamics.

We have thus demonstrated how to use high-harmonic spectroscopy to elucidate a complex photochemical process from the first femtoseconds that are governed by a conical intersection to the picosecond time scale where dissociation proceeds statistically. Our results on the femtosecond dynamics may be used in the future to check high-level quantum dynamical

calculations. We anticipate that this property will be of great value to femtochemistry and ultrafast imaging.

## References and Notes

- E. Goulielmakis *et al.*, *Nature* **466**, 739 (2010).
- L. Nugent-Glandorf *et al.*, *Phys. Rev. Lett.* **87**, 193002 (2001).
- W. Li *et al.*, *Science* **322**, 1207 (2008).
- H. J. Wörner, J. B. Bertrand, D. V. Kartashov, P. B. Corkum, D. M. Villeneuve, *Nature* **466**, 604 (2010).
- H. J. Wörner, J. B. Bertrand, P. B. Corkum, D. M. Villeneuve, *Phys. Rev. Lett.* **105**, 103002 (2010).
- M. Meckel *et al.*, *Science* **320**, 1478 (2008).
- C. Z. Bisgaard *et al.*, *Science* **323**, 1464 (2009).
- W. Domcke, D. R. Yarkony, H. Köppel, Eds., *Conical Intersections: Electronic Structure, Dynamics and Spectroscopy*, vol. 15, *Advanced Series in Physical Chemistry* (World Scientific, Singapore, 2004).
- P. H. Bucksbaum, *Science* **317**, 766 (2004).
- D. Polli *et al.*, *Nature* **467**, 440 (2010).
- T. Schultz *et al.*, *Science* **306**, 1765 (2004).
- G. E. Busch, K. R. Wilson, *J. Chem. Phys.* **56**, 3626 (1972).
- M. Quack, J. Troe, *Ber. Bunsenges. Phys. Chem.* **78**, 240 (1974).
- S. I. Ionov, G. A. Brucker, C. Jaques, Y. Chen, C. Wittig, *J. Chem. Phys.* **99**, 3420 (1993).
- F. Santoro, C. Petrongolo, *J. Chem. Phys.* **110**, 4419 (1999).
- S. Mahapatra, H. Köppel, L. S. Cederbaum, P. Stampfl, W. Wenzel, *Chem. Phys.* **259**, 211 (2000).
- Y. Arasaki, K. Takatsuka, *Chem. Phys.* **338**, 175 (2007).
- Y. Arasaki, K. Takatsuka, K. Wang, V. McKoy, *J. Chem. Phys.* **132**, 124307 (2010).
- I. Wilkinson, B. J. Whitaker, *Annu. Rep. Prog. Chem. Sect. C: Phys. Chem.* **106**, 274 (2010).
- A.-T. Le, R. R. Lucchese, M. T. Lee, C. D. Lin, *Phys. Rev. Lett.* **102**, 203001 (2009).
- M. V. Frolov *et al.*, *Phys. Rev. Lett.* **102**, 243901 (2009).
- J. Itatani *et al.*, *Nature* **432**, 867 (2004).
- T. Morishita, A.-T. Le, Z. Chen, C. D. Lin, *Phys. Rev. Lett.* **100**, 013903 (2008).
- H. J. Wörner, H. Niikura, J. B. Bertrand, P. B. Corkum, D. M. Villeneuve, *Phys. Rev. Lett.* **102**, 103901 (2009).
- H. J. Wörner, J. B. Bertrand, P. Hockett, P. B. Corkum, D. M. Villeneuve, *Phys. Rev. Lett.* **104**, 233904 (2010).
- M. Swoboda *et al.*, *Phys. Rev. Lett.* **104**, 103003 (2010).
- M. Schultze *et al.*, *Science* **328**, 1658 (2010).
- B. Abel, B. Kirmse, J. Troe, D. Schwarzer, *J. Chem. Phys.* **115**, 6522 (2001).
- A. Vredenburg, W. G. Roeterdink, M. H. M. Janssen, *J. Chem. Phys.* **128**, 204311 (2008).
- Y. Mairesse *et al.*, *Phys. Rev. Lett.* **100**, 143903 (2008).
- N. T. Form, B. J. Whitaker, L. Poisson, B. Soep, *Phys. Chem. Chem. Phys.* **8**, 2925 (2006).
- D. Irimia, I. D. Petsalakis, G. Theodorakopoulos, M. H. M. Janssen, *J. Phys. Chem. A* **114**, 3157 (2010).
- J. B. Hamard, R. Cireasa, B. Chatel, V. Blanchet, B. J. Whitaker, *J. Phys. Chem. A* **114**, 3167 (2010).
- J. B. Bertrand *et al.*, *Phys. Rev. Lett.* **106**, 023001 (2011).

**Acknowledgments:** We thank A. Stolow for fruitful discussions and B. Whitaker and K. Takatsuka for permission to use information underlying Figs. 1 and 4C. We acknowledge financial support from the Swiss National Science Foundation (PPOOP2\_128274), Agence Nationale de la Recherche (ANR-08-JCJC-0029 HarmoDyn), Centre National de la Recherche Scientifique (PICS: Imagerie moléculaire par impulsions attosecondes), National Sciences and Engineering Research Council of Canada, Canadian Institute for Photonic Innovations, and Air Force Office of Scientific Research.

## Supporting Online Material

www.sciencemag.org/cgi/content/full/334/6053/208/DC1  
Materials and Methods  
Figs. S1 to S5  
Tables S1 to S6  
References (35–43)

20 May 2011; accepted 15 August 2011  
10.1126/science.1208664



## Supporting Online Material for

### **Conical Intersection Dynamics in NO<sub>2</sub> Probed by Homodyne High-Harmonic Spectroscopy**

H. J. Wörner,\* J. B. Bertrand, B. Fabre, J. Higuët, H. Ruf, A. Dubrouil,  
S. Patchkovskii, M. Spanner, Y. Mairesse, V. Blanchet, E. Mével,  
E. Constant, P. B. Corkum, D. M. Villeneuve

\*To whom correspondence should be addressed. E-mail: woerner@phys.chem.ethz.ch

Published 14 October 2011, *Science* **334**, 208 (2011)  
DOI: 10.1126/science.1208664

#### **This PDF file includes:**

Materials and Methods  
Figs. S1 to S5  
Tables S1 to S6  
References

# 1 Materials and Methods

The experimental setup consists of a chirped-pulse amplified titanium-sapphire laser system (800 nm, 8 mJ, 32 fs, 50 Hz), an optical setup for generation and synchronization of multiple fundamental and second harmonic laser beams and a vacuum chamber for generation and spectral characterization of high-harmonic extreme-ultraviolet radiation.

The output of the laser system is split into two beams of variable intensities using a half-wave plate and a thin-film polarizer. The probe beam is sent through a computer-controlled delay stage. The pump beam is reduced in diameter by a 2:1 reflective telescope and frequency doubled in a BBO crystal of 0.1 or 2 mm thickness. Angle-tuning of the thick BBO crystal enables a limited tuning of the center wavelength of the second harmonic. The 400 nm beam is subsequently divided using a 50:50 beamsplitter and the two resulting beams are recombined with the 800 nm (probe) beam using a dichroic mirror. The 400 nm (pump) beams are vertically separated from the 800 nm (probe) beam by  $\pm 0.75$  cm and the three beams propagate parallel to each other onto a  $f=50$  cm concave aluminum mirror that focuses them into a vacuum chamber equipped with a pulsed gas nozzle.

The nozzle is positioned  $\sim 2$ mm after the focus of the 800 nm pulse to select high harmonics generated from the short electron trajectories. The two 400 nm beams are aligned such that they cross the 800 nm beam at the position where the high harmonics are generated. This is achieved by optimizing the wave-mixing signal described in Ref. (34). We use a supersonic expansion of neat  $\text{NO}_2$ , using a backing pressure of  $\sim 1$  atm and heating the nozzle to  $100^\circ\text{C}$  to suppress the formation of  $\text{N}_2\text{O}_4$ . The generated high-harmonic radiation propagates into a second vacuum chamber where it is spectrally dispersed by a spherical grating and the spectrum is imaged onto a microchannel plate detector backed with a phosphor screen. Spectral images are recorded using a charge-coupled device camera. The ions generated in the interaction region of the laser and gas pulses are collected by means of a copper mesh located 10 cm downstream of the nozzle orifice and the resulting current is detected (5).

## 2 Data analysis

The two pump beams set up a transient grating of intensity as shown in Fig. 2 of the main article:

$$I(x) = I_{\text{av}} (\cos(kx) + 1), \quad (1)$$

where  $k = 2\pi/\Lambda$ ,  $\Lambda = 13.3\mu\text{m}$  is the period of the grating and  $I_{\text{av}}$  is the average of the pump intensity over the dimension  $x$ . One-photon excitation transfers a fraction of the molecules from the ground state (g) into the excited state (e). Consequently, the excitation fraction is also modulated spatially according to

$$r(x) = r (\cos(kx) + 1), \quad (2)$$

where  $r$  is the excitation fraction averaged over  $x$ .

For a given photon energy  $\Omega$  of the high-harmonic spectrum, the emission of the ground state can be written in terms of its amplitude and phase as  $E_g(\Omega) = d_g e^{i\phi_g}$  and the emission of the excited state as  $E_e(\Omega) = d_e e^{i\phi_e}$ . The high-harmonic emission across the transient grating is thus given by

$$\begin{aligned} E(\Omega, x) &= E_g(\Omega, x) + E_e(\Omega, x) \\ &= (1 - r(x))d_g e^{i\phi_g} + r(x)d_e e^{i\phi_e} \\ &= (1 - r)d_g e^{i\phi_g} + r d_e e^{i\phi_e} + r \cos(kx) (d_e e^{i\phi_e} - d_g e^{i\phi_g}). \end{aligned} \quad (3)$$

The high-harmonic emission  $E(\Omega, x)$  thus consists of a term that is independent of  $x$  and one that is proportional to  $\cos(kx)$ . The spectrally resolved far-field harmonic profile is given by the Fourier transform of  $E(\Omega, x)$  which is (4)

$$FT(E(x)) = \left( (1-r)d_g e^{i\phi_g} + r d_e e^{i\phi_e} \right) \delta(\xi) + \frac{r}{2} \left( d_e e^{i\phi_e} - d_g e^{i\phi_g} \right) \left( \delta\left(\xi - \frac{k}{2\pi}\right) + \delta\left(\xi + \frac{k}{2\pi}\right) \right). \quad (4)$$

The observed signal can thus be determined from Eq. (4) to consist of a non-diffracted part of intensity

$$I_{m=0} = \left| (1-r)d_g e^{i\phi_g} + r d_e e^{i\phi_e} \right|^2 \quad (5)$$

and first order diffraction ( $m = \pm 1$ ) of intensity

$$I_{m=\pm 1} = \frac{r^2}{4} \left| d_e e^{i\phi_e} - d_g e^{i\phi_g} \right|^2. \quad (6)$$

The non-diffracted signal thus results from the interference of emissions from the two states, weighted by their populations, whereas the diffracted signal results from interference of the emissions with equal weights. The signal in  $m = 0$  is thus equivalent to what is observed in a collinear pump-probe experiment (5), whereas the diffracted signal enhances the contribution of the excited state.

The spectral images observed for three different delay times between the two synchronized 400 nm (transient grating) pulses and the 800 nm generating pulse are displayed in Fig. S1. Image a) was taken at a negative time delay (800 nm pulse preceding the 400 nm pulse) and only shows the odd harmonics from H11 to H21. Image b) corresponds to temporal overlap of all three pulses and shows, in addition to the odd harmonics, several other frequency components arising from non-linear wave mixing of the three pulses, as described in Ref. (34). Image c) was taken at a positive time delay and shows diffracted high-harmonic radiation above and below each of the odd harmonic orders.

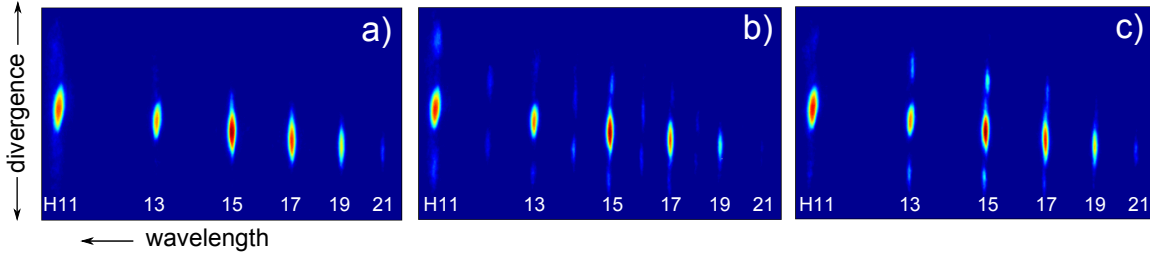


Fig. S1: Frequency-resolved far-field high-harmonic profiles observed from a transient grating experiment in  $\text{NO}_2$ . Panels a, b and c correspond to negative, zero and positive delays between the 400 nm transient grating excitation (pump) pulses and the 800 nm pulse generating the high-harmonic radiation.

### 3 Polarization dependence of pump-probe signals

In experiments using perpendicularly polarized pump and probe pulses, a clear modulation was observed in the diffracted signal, as shown in Fig. 4 of the main article. Figure S2 shows the diffracted and undiffracted high-harmonic signals as a function of the delay between the parallel polarized pump (400 nm) and probe (800 nm) pulses under experimental conditions otherwise similar to those of Fig. 4. The absence of clear modulations from Fig. S2 thus reveals a strong polarization dependence of the modulations in the diffracted high-harmonic signal.

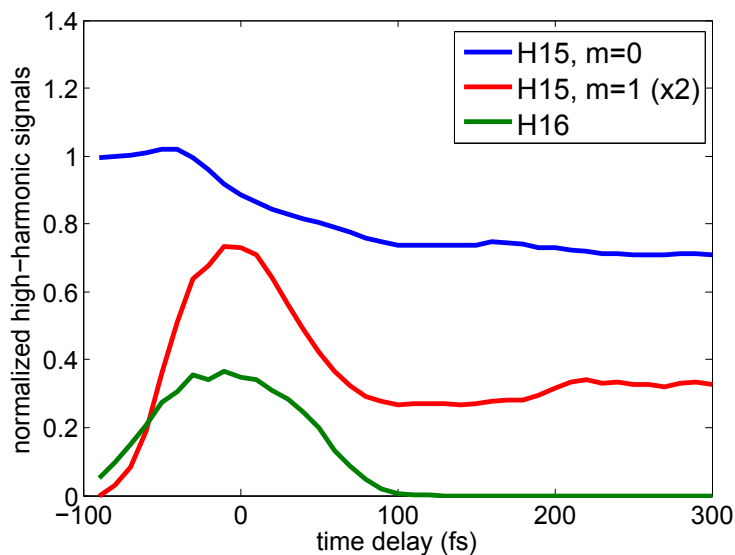


Fig. S2: High-harmonic yields as a function of the delay between a 401 nm pump pulse and an 800 nm probe pulse generating high-harmonics in the excited sample. The figure shows the yield of diffracted (red line) and undiffracted (blue line) high-harmonic signals, normalized to the undiffracted signal at negative pump-probe delays. The polarizations of pump and probe pulses were parallel. The pulse energy of the exciting pulses was 10  $\mu$ J.

## 4 Excluding contributions from $N_2O_4$

The absence of a clear modulation in the case of parallel polarized pulses shown in Fig. S2 has an additional importance. A molecular expansion of  $NO_2$  unavoidably contains traces of  $N_2O_4$ , although we have heated the nozzle to 100 °C to suppress the dimer formation. The vibrational period of the most strongly Raman active mode of  $N_2O_4$  is 130 fs, which is close to the modulation observed here (3). However, vibrational wave packet motion has been observed by HHG in  $N_2O_4$  and found to be much more pronounced in the case of parallel polarized pulses than in the cross-polarized case. The comparison of the results of the two polarization geometries thus enables us to exclude the contribution of dimer vibrations to the observed signal.

## 5 Excluding contributions from the ionization step

The modulations observed in the diffracted high-harmonic signal in Fig. 4 of the main article might be caused by a variation of the strong-field-ionization rate of the molecule as a function of the nuclear coordinates. To rule out this possibility we have measured the total ion yield in parallel to the high-harmonic yield and have not observed any modulation on top of the smooth increase as shown in Fig. S3. A comparison of the signal-to-noise ratios of the diffracted high-harmonic and ion yield measurement allows us to exclude a variation in the ionization rate as the origin of the observed modulations.

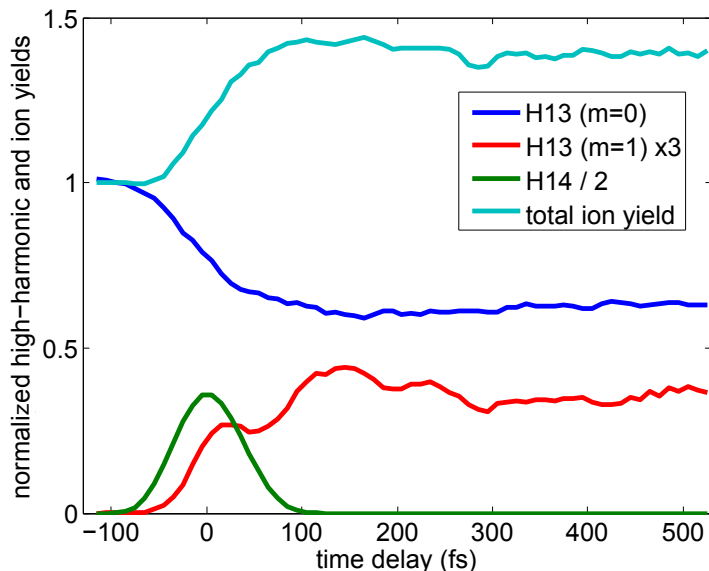


Fig. S3: High-harmonic and ion yields as a function of the delay between a 401 nm pump pulse and an 800 nm probe pulse generating high harmonics in the excited sample. The figure shows the yield of diffracted (red line), undiffracted (dark blue line) high-harmonic signals and total ion yields (light blue line), normalized to the undiffracted signals at negative pump-probe delays. The polarizations of pump and probe pulses were perpendicular.

## 6 Quantum chemistry calculations

We performed quantum chemical calculations of  $\text{NO}_2$  at three geometries: (1)  $134^\circ$  angle corresponding to the ground state equilibrium geometry and to the outer turning point of the wave packet on the diabatic  $\tilde{A}^2B_2$  state; (2)  $102^\circ$  angle corresponding to the saddle point of the diabatic  $\tilde{A}^2B_2$  state; and (3)  $85^\circ$  angle corresponding to the inner turning point of the wave packet on the diabatic  $\tilde{A}^2B_2$  state. At each geometry, we calculate (1) strong-field-ionization yield and its angular variation; (2) Dyson orbital corresponding to each ionization channel; (3) recombination transition dipole moment between the cation and the neutral states.

All electronic structure calculations were performed in GAMESS-US (35), using Complete Active Space (CAS) wavefunctions, with 17 electrons in 12 active orbitals. A spherical Gaussian valence triple-zeta quality basis set, augmented with diffuse basis functions (aug-cc-pVTZ (36, 37)) was used on all atoms. Strong-field ionization calculations were performed at the optimized pure-state CAS geometry of the  $\tilde{X}^2A_1$  state ( $r_{N-O} = 1.204 \text{ \AA}$ ;  $\alpha_{O-N-O} = 133.9^\circ$ ), at the  $\tilde{A}^2B_2$  saddle point ( $r_{N-O} = 1.269 \text{ \AA}$ ;  $\alpha_{O-N-O} = 101.7^\circ$ ) of the  $\tilde{A}^2A'$  excited state, and at the approximate inner turning point on the  $\tilde{A}^2B_2$ , ( $\alpha_{O-N-O} = 85^\circ$ ). The geometries are defined in Table S1.

Dyson orbitals and ionic Hartree potentials were evaluated (38) from the pure-state CAS(17,12) wavefunctions for the neutral  $\text{NO}_2$  and equally-weighted, mixed-spin 3-state-averaged CAS(16,12) cation wavefunctions. Calculated relative energies of the low-lying electronic states of  $\text{NO}_2$  and  $\text{NO}_2^+$  at the three geometries are summarized in Table S2. Note that only the lowest state in each of the four irreducible representations was determined for the neutral species. The present CAS calculations do not include dynamical correlations and consistently underestimate the ionization potential of  $\text{NO}_2$  ( $^1A_1 \leftarrow ^2A_1$

vertical ionization potential is 11.23 eV experimentally (39)). However, the relative ionization potentials of the different channels are expected to be well reproduced.

Strong-field ionization rates were calculated within an uncoupled single-channel approach (40). The ionizing field was a half-cycle  $\sin^2$  pulse with the peak intensity of  $10^{14}$  W/cm<sup>2</sup> ( $E_{max} = 0.05345$  a.u.), with the second time derivative of  $E$  at the field maximum chosen to match the shape of the 800-nm field maximum. The simulation was continued for 12 atomic units of time (au[t]) after the field turn-off, for the total of 90 au[t] (2.18 fs), to let ionized electrons reach the absorbing boundaries. The time step in leap-frog propagation of the wavefunction was 0.003 au[t]. The cubic simulation box extended to  $\pm 18$  Bohr in each direction. The Cartesian grid spacing was 0.15 Bohr. A reflection-free complex absorbing potential (41) extended 9.4 Bohr from the grid boundary. Angular dependence of the total photoelectron yield on the laser field polarization was calculated on the 38-point 9th-order Lebedev grid (42), then interpolated with spherical harmonics with angular momentum  $L \leq 5$ .

Calculated square norms of the Dyson orbitals, corresponding to the low-lying ionization channels at the three representative geometries are summarized in Table S3. Dyson orbital norms close to one indicate that an ionization channel is allowed as a single-electron transition (Koopmans' correlation-allowed channel). Values close to zero indicate that electronic rearrangement within the ion core must accompany an electron removal. For ionization channels where strong field ionization yields were calculated, total photoelectron yield for a randomly oriented sample is also given in Table S3. The shapes of the Dyson orbitals and the polarization dependence of the total photoelectron yield are illustrated in Fig. S5.

In the experiment, population on the  $\tilde{A}^2B_2$  was produced by a laser pulse centered in the vicinity of 400 nm. At the equilibrium geometry of the  $\tilde{X}^2A_1$  ground state of the NO<sub>2</sub> radical, the strongest single-photon dipole-allowed electronic excitation is to the  $\tilde{A}^2A'$  ( $\tilde{A}^2B_2$  at the C<sub>2v</sub> geometry) state. The transition moment lies along the O-O direction, so that the pump pulse creates a partially aligned population of the  $\tilde{A}^2A'$  state. Simultaneously, the population of NO<sub>2</sub> in the  $\tilde{X}^2A_1$  is weakly depleted for molecules with the O-O axis along the pump field.

Figure S4 shows the potential energies for the important states as a function of the bend angle, derived from Ref. (18). We consider high-harmonic generation from the three geometries described above. The most probable transitions are labeled as channels #1-#7.

The Dyson orbitals and the angular variation of the strong-field photoionization probability are shown in Fig. S5. Only the Dyson orbitals corresponding to removal of a  $b_2$  electron (channels #2, 4 and 6) are significantly different from the Dyson orbital of the unexcited molecules (channel 1).

Dipole matrix elements for the bound-continuum transitions were calculated in the eikonal single active-electron approximation (43). Eikonal scattering states were calculated in the Coulomb (nuclear attraction and Hartree repulsion) potential of the appropriate ion core, and are normalized to unit electron density. The target recombination channel is represented by the corresponding Dyson orbital. Orthogonalization and exchange effects involving the ion core are treated as described in Ref. (38). The calculation was performed on a uniformly-spaced Cartesian grid (grid spacing of 0.15 Bohr) extending to  $\pm 18$  Bohr from the coordinate origin. The transition dipoles are shown in Table S4. They are evaluated for an electron kinetic energy of 20 eV, about the maximum of each curve; this corresponds to a photon energy of about 30 eV close to harmonic order 19.

We now estimate the emitted signal from each channel. Table S4 summarizes the calculations for the three geometries. Tables S5 and S6 summarize the predictions of the emission for each channel for perpendicular and parallel laser polarizations. The column labeled Product is the relative amplitude of the emission, and is the product of the previous columns as indicated in the caption. For channels with non-zero signal, the radiated dipole shows both the amplitude and phase of the emitted electric field. The phase is determined by both the recombination dipole phase and the propagation phase ( $\phi = \Delta I_p \tau$ )

due to the difference  $\Delta I_p$  in ionization potentials and the transit time of the electron in the continuum  $\tau \approx 1.7$  fs (70 atomic units) for the highest harmonics.

The intensity of the high-harmonic emission that is diffracted into the first order of the transient grating is defined in the main text in eq. 4, which we repeat here.

$$I_{m=1}(\Omega, t) = \frac{1}{4} \left| r_{\tilde{A}}(t)(d_{\tilde{A}}e^{i\phi_{\tilde{A}}} - d_g e^{i\phi_g}) + r_{\tilde{X}}(t)(d_{\tilde{X}}e^{i\phi_{\tilde{X}}} - d_g e^{i\phi_g}) \right|^2. \quad (7)$$

We first study the sensitivity of the diffracted signal to the populations of the two diabatic states at the three characteristic geometries and then show that even in the case of a complete delocalization of the wave packet (as is essentially the case for a 40 fs excitation pulse), the diffraction is still sensitive to the population in the diabatic states. The following table summarizes the results for single geometries:

$$I_{m=1}(134^\circ, \text{perpendicular}) = \frac{1}{4} \left| r_A(95e^{-i3.3} - 52) + r_X(52 - 52) \right|^2 = 5371r_A^2 \quad (8)$$

$$I_{m=1}(134^\circ, \text{parallel}) = \frac{1}{4} \left| r_A(0 - 52) + r_X(5.2e^{i7.6} - 52) \right|^2 = 676r_A^2 + 1012r_X^2 + 1318r_A r_X \quad (9)$$

$$I_{m=1}(102^\circ, \text{perpendicular}) = \frac{1}{4} \left| r_A(69e^{i2.36} - 52) + r_X(0 - 52) \right|^2 = 3140r_A^2 + 676r_X^2 + 2940r_A r_X \quad (10)$$

$$I_{m=1}(102^\circ, \text{parallel}) = \frac{1}{4} \left| r_A(0 - 52) + r_X(10e^{i3.08} - 52) \right|^2 = 676r_A^2 + 961r_X^2 + 1611r_A r_X \quad (11)$$

$$I_{m=1}(85^\circ, \text{perpendicular}) = \frac{1}{4} \left| r_A(46e^{i5.35} - 52) + r_X(0 - 52) \right|^2 = 493r_A^2 + 676r_X^2 + 640r_A r_X \quad (12)$$

$$I_{m=1}(85^\circ, \text{parallel}) = \frac{1}{4} \left| r_A(8.5e^{-i0.67} - 52) + r_X(0 - 52) \right|^2 = 520r_A^2 + 676r_X^2 + 1179r_A r_X \quad (13)$$

First, let us examine the case of perpendicular laser polarizations. It can be seen that the model predicts that the diffracted high-harmonic signal at the outer turning point ( $134^\circ$ ) is determined by the population in the  $\tilde{A}^2B_2$  state alone. In the  $102^\circ$  geometry (near the conical intersection), it can be seen that there is also a contribution from the  $\tilde{X}^2A_1$  population, but the  $\tilde{A}^2B_2$  still dominates. Bent geometries lower than  $95^\circ$  are not visited by the  $\tilde{X}^2A_1$  wave packet at 3 eV of total excitation energy. Consequently, at the inner turning point of the  $\tilde{A}^2B_2$  ( $85^\circ$ ) both the  $\tilde{A}^2B_2$  and the unexcited  $\tilde{X}^2A_1$  contribute equally. For the case of parallel polarizations, both states contribute about equally at all geometries.

Using the radiated dipoles in Tables S5 and S6, we now turn to estimate  $I_{m=1}$  for perpendicular and parallel laser polarizations for a delocalized wave packet. We are evaluating how the wavepacket population in the  $\tilde{X}^2A_1$  and  $\tilde{A}^2B_2$  states contribute to the diffracted HHG signal. We estimate the emission from each surface by taking the average of the dipole at each of the three geometries in Tables S5 and S6. The two polarization cases are shown in eqs. (14)-(15).

We can estimate the sensitivity of the diffracted signal to  $r_A$  and  $r_X$  by taking differentials, shown in eqs. (16)-(17); we assume that  $r_A = r_X = 0.1$  for the purpose of this estimate.

This shows that the diffracted signal is about 2.6 times more sensitive to population in  $\tilde{A}^2B_2$  than in  $\tilde{X}^2A_1$  when the laser polarizations are perpendicular. When the laser polarizations are parallel, the contributions to the diffracted signal are equal from both states. This agrees with the experimental observation that modulation of the  $I_{m=1}$  signal is only seen for perpendicular polarizations. Therefore our model supports the conclusion that the high-harmonic-spectroscopy experiment is measuring the population in the diabatic  $\tilde{A}^2B_2$  state. This simple model justifies this conclusion, but the strongest

$$\begin{aligned}
I_{m=1}(\text{perpendicular}) &= \frac{1}{4} \left| r_A \left( \frac{1}{3} (95e^{-i3.3} + 69e^{i2.36} + 46e^{i5.35}) - 52 \right) + r_X \left( \frac{1}{3} (52 + 0 + 0) - 52 \right) \right|^2 \\
&= 2066r_A^2 + 300r_X^2 + 1568r_Ar_X \tag{14}
\end{aligned}$$

$$\begin{aligned}
I_{m=1}(\text{parallel}) &= \frac{1}{4} \left| r_A \left( \frac{1}{3} (0 + 0 + 8.5e^{-i0.67}) - 52 \right) + r_X \left( \frac{1}{3} (5.2e^{i7.6} + 10e^{i3.08} + 0) - 52 \right) \right|^2 \\
&= 620r_A^2 + 754r_X^2 + 1365r_Ar_X \tag{15}
\end{aligned}$$

$$dI_{m=1}(\text{perpendicular}) = 569dr_A + 216dr_X \tag{16}$$

$$dI_{m=1}(\text{parallel}) = 260dr_A + 287dr_X \tag{17}$$

evidence is the good agreement between the experiment and the detailed calculations of Arasaki et al. (18).

Finally, let us see if our simple model agrees with the magnitude of the modulation of the diffracted signal, shown in Fig. 4B of the main article. We start with the calculated  $\tilde{A}^2B_2$  population of Arasaki et al. (18), shown in Fig. 4C. We assume that our total excited state population fraction is 0.15, as shown in Table 1 in the main text, and so  $r_A + r_X = 0.15$ . Scaling Fig. 4C to this value, we associate the first peak with  $r_A = 0.09$  and  $r_X = 0.06$ . The subsequent valley will have  $r_A = 0.06$  and  $r_X = 0.09$ . We then substitute these values into eqs. (14)-(15), and scale the results vertically to match Fig. 4B. For perpendicular polarization, our model predicts that the first peak on Fig. 4B should be 0.64 and the first valley should be 0.45; this is a somewhat greater modulation than what was actually observed, but is quite close. For parallel polarizations, this simple model predicts a signal of 0.36 at the first peak and 0.37 at the first valley, i.e. it predicts that there is no modulation of the signal, as was observed experimentally.

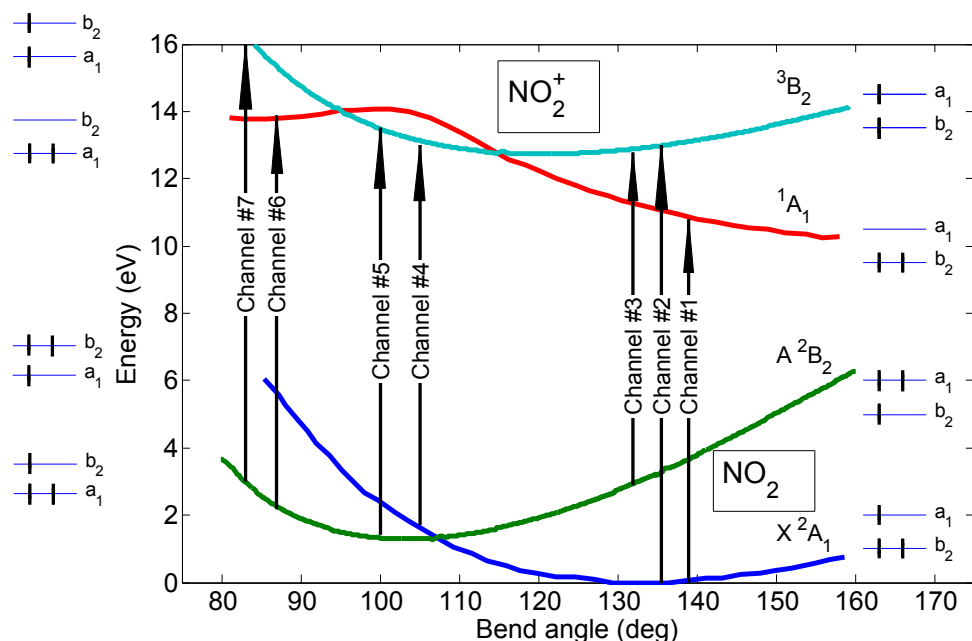


Fig. S4: Potential energy diagram of the relevant states of  $\text{NO}_2$  and  $\text{NO}_2^+$ , derived from Ref. (18). The primary strong-field ionization channels that lead to HHG are shown as arrows. Each channel is referred to in the text as channel #1-#7. Note that the energetic ordering of the  $a_1$  and  $b_2$  orbitals changes as a function of the bending angle.

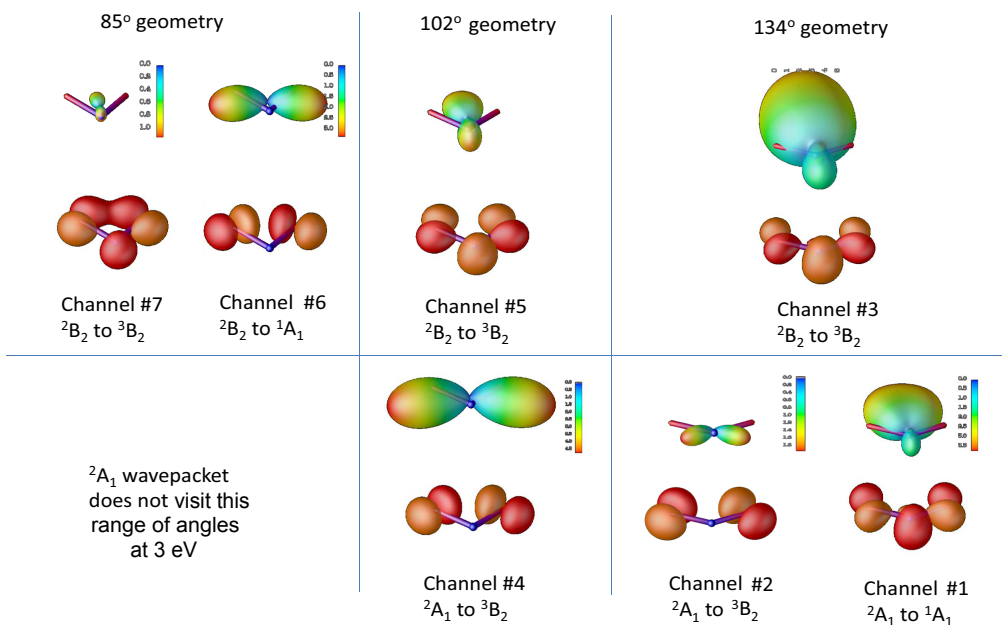


Fig. S5: Dyson orbitals and angular variation of strong-field ionization probabilities for each of the seven primary HHG channels. The Dyson orbitals are at the bottom of each panel, whereas the photoionization probability distributions are at the top of each panel. The channel labels are defined in Fig. S4. For the integrated ionization probability for each channel, see Table S1.

Table S1: Coordinates of the nuclei used for strong-field ionization simulations. Cartesian coordinates are given in Angstroms.

Atom $Z_{nuc}$	Coordinates (Å)		
	X	Y	Z
$134^\circ \ ^2A_1$ geometry			
7.00	0.00000	0.00000	-0.11398
8.00	0.00000	-1.10809	0.35699
8.00	0.00000	1.10809	0.35699
$102^\circ \ ^2B_2$ geometry			
7.00	0.00000	0.00000	-0.33393
8.00	0.00000	-0.98428	0.46696
8.00	0.00000	0.98428	0.46696
$85^\circ \ ^2B_2$ geometry			
7.00	0.00000	0.00000	-0.45098
8.00	0.00000	-0.88809	0.51820
8.00	0.00000	0.88809	0.51820

Table S2: Energies of the low-lying electronic states of NO<sub>2</sub> and NO<sub>2</sub><sup>+</sup>, in electron-Volts, relative to the energy of 1<sup>2</sup>A<sub>1</sub> state at its optimized geometry, at the CASSCF(17,12)//aug-ccpVTZ level of theory. The energies of all ionic states need to be increased by 1.68 eV to match the experimental vertical ionization energy.

Geometry	R (Å)	Angle (°)	State	E (eV)
1 <sup>2</sup> A <sub>1</sub>	1.2040	133.9	<sup>2</sup> A <sub>1</sub>	0.000
134°	neutral		<sup>2</sup> B <sub>1</sub>	2.907
			<sup>2</sup> B <sub>2</sub>	3.234
			<sup>2</sup> A <sub>2</sub>	3.381
	cation		<sup>1</sup> A <sub>1</sub>	9.548
			<sup>3</sup> B <sub>2</sub>	11.500
			<sup>3</sup> A <sub>2</sub>	12.065
1 <sup>2</sup> B <sub>2</sub>	1.2690	101.7	<sup>2</sup> B <sub>2</sub>	1.160
102°	neutral		<sup>2</sup> A <sub>1</sub>	1.880
			<sup>2</sup> A <sub>2</sub>	2.091
			<sup>2</sup> B <sub>1</sub>	4.803
	cation		<sup>3</sup> B <sub>2</sub>	11.812
			<sup>1</sup> A <sub>1</sub>	12.322
			<sup>3</sup> B <sub>1</sub>	13.042
1 <sup>2</sup> B <sub>2</sub>	1.3146	85.0	<sup>2</sup> B <sub>2</sub>	1.925
85°	neutral		<sup>2</sup> A <sub>2</sub>	3.848
			<sup>2</sup> B <sub>1</sub>	3.891
			<sup>2</sup> A <sub>1</sub>	4.669
	cation		<sup>1</sup> A <sub>1</sub>	12.257
			<sup>3</sup> B <sub>1</sub>	13.064
			<sup>3</sup> B <sub>2</sub>	13.585

Table S3: Square of the Dyson orbital norms and strong-field-ionization yields for the three geometries considered. Total yield for a half cycle of 800 nm linearly polarized laser field at the peak intensity of  $10^{14}$  W/cm<sup>2</sup>.

Geometry	Neutral State	Cation State	Dyson norm <sup>2</sup>	Ionization Yield ( $10^{-4}$ )	Channel Label
$\tilde{X}^2A_1$ 134°	$^2A_1$	$^1A_1$	0.861	15.8	#1
		$^3B_2$	0.878	7.74	#2
		$^3A_2$	0.858		
	$^2B_2$	$^1A_1$	0.019	1.61	
		$^3B_2$	0.842	37.2	#3
		$^3A_2$	0.020		
$\tilde{A}^2B_2$ 102°	$^2B_2$	$^3B_2$	0.867	15.2	#5
		$^1A_1$	0.506	3.01	
		$^3B_1$	0.836		
	$^2A_1$	$^3B_2$	0.834	21.6	#4
		$^1A_1$	0.326	2.73	
		$^3B_1$	0.030		
85°	$^2B_2$	$^1A_1$	0.801	10	#6
		$^3B_2$	0.856	6.1	#7
		$^3B_1$	0.837	5	

Table S4: Summary of calculated results for the three geometries considered. For each geometry, the most significant channel for ionization from the ground and excited electronic states is shown. The directions for the ionization ( $P_{ion}$ ) and recombination dipole moment ( $d$ ) are: Z is parallel to the  $C_2$  symmetry axis, and Y is parallel to the O-O axis as shown in Fig. 1 of the main article. The transition moment of the pump step is parallel to Y. When pump and probe pulses are cross-polarized, ionization and recombination take place along Z. In the case of parallel polarizations, ionization and recombination occur along Y.

Channel	Transition	$P_{ion}$	Dyson <sup>2</sup>	$d$ ampl	$d$ phase (rad)	$I_p$ (eV)
#1	$^1A_1 \leftarrow ^2A_1$	16 Z	0.86	14 Z	0	11.15
#2	$^3B_2 \leftarrow ^2A_1$	7.7 Y	0.88	2 Y	2.9	13.0
#3	$^3B_2 \leftarrow ^2B_2$	37 Z	0.84	17 Z	0.2	9.78
#4	$^3B_2 \leftarrow ^2A_1$	22 Y	0.83	2.5 Y	2.8	11.26
#5	$^3B_2 \leftarrow ^2B_2$	15 Z	0.87	19 Z	0.1	12.03
#6	$^1A_1 \leftarrow ^2B_2$	10 Y	0.80	3 Y	-0.9	11.20
#7	$^3B_2 \leftarrow ^2B_2$	6.1 Z	0.86	20 Z	0.1	13.19

Table S5: Summary of calculated results for the three geometries considered. The polarizations of pump and probe laser pulses are **perpendicular** to each other. For each channel, molecules that have their O-O axes aligned either parallel or perpendicular to the pump laser polarization are shown. The Excitation column indicates whether the pump laser excites the molecule for that orientation. The next columns contain numbers from Table S4. The column labeled "Product" is the product of the columns to the left: Product = Excitation  $P_{ion}^{1/2}$  Dyson Dipole.  $\Delta I_p \tau = (I_p - I_p(ref))70(at.un.)$  is the phase shift of the high-harmonic radiation relative to the unexcited ground state due to the differing ionization potentials.

Channel	Orientation	Excitation	$P_{ion}$	Dyson <sup>2</sup>	Dipole	Product	$\Delta I_p \tau$ (rad)	Radiated Dipole
134° geometry								
#1		1	16	0.86	14	52	0	$d_g = 52$
	⊥	0	0	0.86	0	0	0	$d_X = 52$
#2		1	0	0.88	0	0	4.7	$d_X = 0$
	⊥	0	7.7	0.84	$2e^{i2.9}$	0	4.7	
#3		1	37	0.84	$17e^{i0.2}$	$95e^{i0.2}$	-3.5	$d_A = 95e^{-i3.3}$
	⊥	0	0	0.84	0	0	-3.5	
102° geometry								
#4		1	0	0.83	0	0	0.28	$d_X = 0$
	⊥	0	22	0.83	$2.5e^{i2.8}$	0	0.28	
#5		1	15	0.87	$19e^{i0.1}$	$69e^{i0.1}$	2.26	$d_A = 69e^{i2.36}$
	⊥	0	0	0.87	0	0	2.26	
85° geometry								
#6		1	0	0.80	0	0	0.13	$d_X = 0$
	⊥	0	10	0.80	$3e^{-i0.9}$	0	0.13	$d_A = 0$
#7		1	6.1	0.86	$20e^{i0.1}$	$46e^{i0.1}$	5.25	$d_A = 46e^{i5.35}$
	⊥	0	0	0.86	0	0	5.25	

Table S6: Summary of calculated results for the three geometries considered. The polarizations of pump and probe laser pulses are **parallel** to each other. For each channel, molecules that have their O-O axes are oriented either parallel or perpendicular to the pump laser polarization are shown. The Excitation column indicates whether the pump laser excites the molecule for that orientation. The next columns contain numbers from Table S4. The column labeled Product is the product of the columns to the left: Product = Excitation  $P_{ion}^{1/2}$  Dyson Dipole.  $\Delta I_p \tau = (I_p - I_p(ref))70(at.un.)$  is the phase shift of the high-harmonic radiation relative to the unexcited ground state due to the differing ionization potentials.

Channel	Orientation	Excitation	$P_{ion}$	Dyson <sup>2</sup>	Dipole	Product	$\Delta I_p \tau$ (rad)	Radiated Dipole
134° geometry								
#1		1	0	0.86	0	0	0	$d_g = 52$
	⊥	0	16	0.86	14	0	0	$d_X = 0$
#2		1	7.7	0.88	$2e^{i2.9}$	$5.2e^{i2.9}$	4.7	$d_X = 5.2e^{i7.6}$
	⊥	0	0	0.84	0	0	4.7	
#3		1	0	0.84	0	0	-3.5	
	⊥	0	37	0.84	$17e^{i0.2}$	0	-3.5	$d_A = 0$
102° geometry								
#4		1	22	0.83	$2.5e^{i2.8}$	$10e^{i2.8}$	0.28	$d_X = 10e^{i3.08}$
	⊥	0	0	0.83	0	0	0.28	
#5		1	0	0.87	0	0	2.26	$d_A = 0$
	⊥	0	15	0.87	$19e^{i0.1}$	0	2.26	
85° geometry								
#6		1	10	0.80	$3e^{-i0.9}$	$8.5e^{-i0.9}$	0.13	$d_X = 0$ $d_A = 8.5e^{-i0.67}$
	⊥	0	0	0.86	0	0	0.13	
#7		1	0	0.86	0	0	5.25	$d_A = 0$
	⊥	0	6.1	0.86	$20e^{i0.1}$	0	5.25	

## References

1. E. Goulielmakis *et al.*, *Nature* **466**, 739 (2010).
2. L. Nugent-Glandorf *et al.*, *Phys. Rev. Lett.* **87**, 193002 (2001).
3. W. Li *et al.*, *Science* **322**, 1207 (2008).
4. H. J. Wörner, J. B. Bertrand, D. V. Kartashov, P. B. Corkum, D. M. Villeneuve, *Nature* **466**, 604 (2010).
5. H. J. Wörner, J. B. Bertrand, P. B. Corkum, D. M. Villeneuve, *Phys. Rev. Lett.* **105**, 103002 (2010).
6. M. Meckel *et al.*, *Science* **320**, 1478 (2008).
7. C. Z. Bisgaard *et al.*, *Science* **323**, 1464 (2009).
8. W. Domcke, D. R. Yarkony, H. Köppel, Eds., *Conical Intersections: Electronic Structure, Dynamics and Spectroscopy*, vol. 15 of *Adv. Ser. in Phys. Chem.* (World Scientific, Singapore, 2004).
9. P. H. Bucksbaum, *Science* **317**, 766 (2007).
10. D. Polli *et al.*, *Nature* **467**, 440 (2010).
11. T. Schultz *et al.*, *Science* **306**, 1765 (2004).
12. G. E. Busch, K. R. Wilson, *J. Chem. Phys.* **56**, 3626 (1972).
13. M. Quack, J. Troe, *Ber. Bunsenges. Phys. Chem* **78**, 240 (1974).
14. S. I. Ionov, G. A. Brucker, C. Jaques, Y. Chen, C. Wittig, *J. Chem. Phys.* **99**, 3420 (1993).
15. F. Santoro, C. Petrongolo, *J. Chem. Phys.* **110**, 4419 (1999).
16. S. Mahapatra, H. Köppel, L. S. Cederbaum, P. Stampfuhl, W. Wenzel, *Chem. Phys.* **259**, 211 (2000).
17. Y. Arasaki, K. Takatsuka, *Chem. Phys.* **338**, 175 (2007).
18. Y. Arasaki, K. Takatsuka, K. Wang, V. McKoy, *J. Chem. Phys.* **132**, 124307 (2010).
19. I. Wilkinson, B. J. Whitaker, *Annu. Rep. Prog. Chem. Sect. C: Phys. Chem.* **106**, 274 (2010).
20. A.-T. Le, R. R. Lucchese, M. T. Lee, C. D. Lin, *Phys. Rev. Lett.* **102**, 203001 (2009).
21. M. V. Frolov *et al.*, *Phys. Rev. Lett.* **102**, 243901 (2009).
22. J. Itatani *et al.*, *Nature* **432**, 867 (2004).
23. T. Morishita, A.-T. Le, Z. Chen, C. D. Lin, *Phys. Rev. Lett.* **100**, 013903 (2008).
24. H. J. Wörner, H. Niikura, J. B. Bertrand, P. B. Corkum, D. M. Villeneuve, *Phys. Rev. Lett.* **102**, 103901 (2009).
25. Y. Mairesse *et al.*, *J. Phys. At. Mol. Opt. Phys.* **43**, 065401 (2010).
26. M. Swoboda *et al.*, *Phys. Rev. Lett.* **104**, 103003 (2010).

27. M. Schultze *et al.*, *Science* **328**, 1658 (2010).
28. P. I. Ionov, I. Bezel, S. I. Ionov, C. Wittig, *Chem. Phys. Lett.* **272**, 257 (1997).
29. A. Vredenburg, W. G. Roeterdink, M. H. M. Janssen, *J. Chem. Phys.* **128**, 204311 (2008).
30. Y. Mairesse *et al.*, *Phys. Rev. Lett.* **100**, 143903 (2008).
31. N. T. Form, B. J. Whitaker, L. Poisson, B. Soep, *Phys. Chem. Chem. Phys.* **8**, 2925 (2006).
32. D. Irimia, I. Petsalakis, G. Theodorakopoulos, M. Janssen, *J. Phys. Chem. A* **xxx**, xxx (2009).
33. J. B. Hamard, R. Cireasa, B. Chatel, V. Blanchet, B. J. Whitaker, *J. Phys. Chem. A* **114**, 3167 (2010).
34. J. B. Bertrand *et al.*, *Phys. Rev. Lett.* **106**, 023001 (2011).
35. M. W. Schmidt *et al.*, *J. Comput. Chem.* **14**, 1347 (1993).
36. T. H. Dunning, Jr., *J. Chem. Phys.* **90**, 1007 (1989).
37. R. A. Kendall, T. H. Dunning, Jr., R. J. Harrison, *J. Chem. Phys.* **96**, 6796 (1992).
38. S. Patchkovskii, Z. Zhao, T. Brabec, D. M. Villeneuve, *J. Chem. Phys.* **126**, 114306 (2007).
39. S. Katsumata, H. Shiromaru, K. Mitani, *Chem. Phys.* **69**, 423 (1982).
40. M. Spanner, S. Patchkovskii, *Phys. Rev. A* **80**, 063411 (2009).
41. D. E. Manolopoulos, *J. Chem. Phys.* **117**, 9552 (2002).
42. V. I. Lebedev, *Zh. Vych. Mat. Mat. Phys.* **15**, 48 (1975).
43. O. Smirnova, M. Spanner, M. Ivanov, *Phys. Rev. A* **77**, 033407 (2008).